Catalyst Self-Assembly Accelerates Bimetallic Light-Driven Electrocatalytic H_2 Evolution in Water

Isaac N. Cloward, Tianfei Liu, Jamie Rose, Annabell G. Bonn, Tamara Jurado, Matthew B. Chambers, Catherine L. Pitman, Marc A. ter Horst, and Alexander J. M. Miller*

Department of Chemistry, University of North Carolina at Chapel Hill, Chapel Hill, NC 27599 (USA)

* Corresponding author: ajmm@email.unc.edu (A.J.M.M.)

Abstract. Hydrogen evolution is an important fuel-generating reaction that has been subject to mechanistic debate about the roles of monometallic and bimetallic pathways. In this study, molecular iridium catalysts that undergo photoelectrochemical dihydrogen evolution afford a rare opportunity to systematically understand the factors that promote bimetallic H–H coupling. Covalently tethered diiridium catalysts evolve H_2 from neutral water faster than monometallic catalysts, even at lower overpotential. The origin of this improvement is noncovalent supramolecular self-assembly into "all-catalyst" nanoscale aggregates that efficiently harvest light and form H–H bonds. New monometallic catalysts containing long-chain alkane substituents leverage the self-assemly to evolve H_2 from neutral water close to the expected maximum rate for a light-driven water splitting reaction and with activity even below 100 mV overpotential. Design parameters for holding multiple catalytic sites in close proximity and tuning catalyst microenvironment emerge from this work.

Introduction

The light-driven transformation of water into dihydrogen and dioxygen holds promise as a sustainable route to synthetic fuel.[1–4] Molecular catalysts for H_2 evolution have been synthetically tuned to achieve exceptional activity and/or low overpotentials, or even to perform both light harvesting and H–H bond formation in a single component to achieve integrated photoelectrocatalysis.[5–10] Molecular catalysts are prime subjects for mechanistic interrogation, which can guide ligand design choices and bring fundamental insight into bond-forming pathways. An enduring mechanistic question encountered in all types of H_2 evolution catalysis pertains to the mode of H–H bond formation. A metal hydride is usually invoked as a pivotal intermediate, which can follow either of two limiting reaction pathways shown in Figure 1: bimetallic coupling of two M–H units (often called the "homolytic" pathway), or monometallic protonolysis of M–H by H^+ ("heterolytic" pathway).[11] Bimetallic pathways promise lower overpotentials and/or high activity under less acidic conditions. Yet, bimetallic examples remain rare. The heavily studied cobaloxime-type H_2 evolution catalysts has been subject of spirited mechanistic debate,[12] but usually favors monometallic pathways (even in covalently linked dicobaloximes).[13] Nickel tetraphenylporphyrin complexes with minimal steric bulk are a rare example in which homolytic H–H coupling dominates.[14,15]

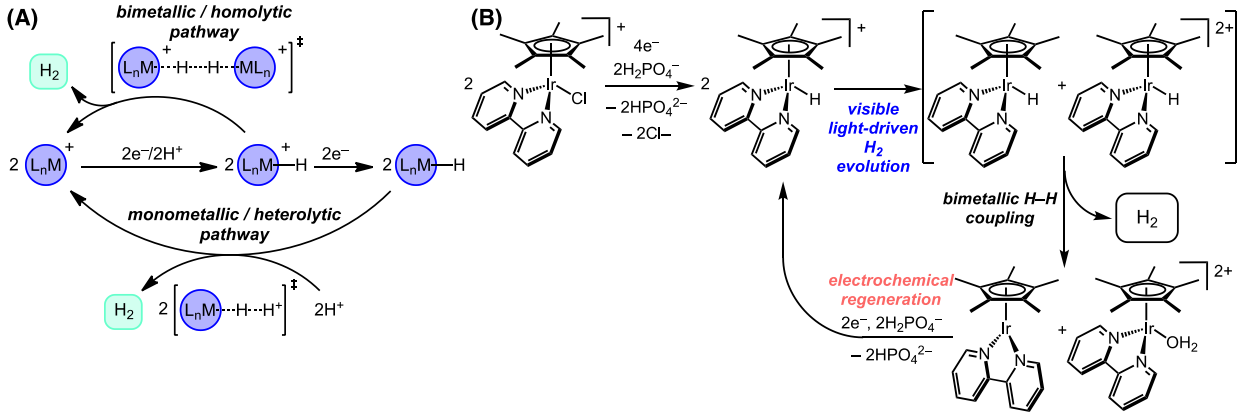

Figure 1. Mechanisms of H_2 evolution. (A) Overview of bimetallic (homolytic) and monometallic (heterolytic) pathways for H_2 evolution. **(B)** Proposed mechanism of H_2 evolution photoelectrocatalysis by the single-component catalyst $[Cp^*Ir(bpy)Cl]^+$.

We recently reported that $[Cp^*Ir(bpy)Cl]^+$ and its analogues are single-component catalysts for light-driven electrochemical H_2 evolution from water at near-neutral pH.[9,16] Integrating light-harvesting and H–H bond formation in a single molecular system can lead to efficient solar-to-fuel reactions, without relying on semiconductors, secondary chromophores, or sacrificial chemical reductants.[9,17–20] Mechanistic studies indicate that an electrochemically generated iridium hydride is photoexcited to a triplet state that undergoes "self-quenching" with a second ground-state iridium hydride, followed by bimetallic H–H coupling (Figure 1B).[21] The iridium photoelectrocatalyst is a rare example of an H_2 evolution catalyst that operates exclusively by a bimetallic mechanism,[15] an thus an ideal platform for understanding how to enhance bimetallic catalysis.

The evolution of molecular designs aimed at promoting bimetallic H–H coupling are described here. The bimetallic H–H coupling mechanism inspired a series of covalently linked bimetallic complexes, hypothesized to efficiently release H_2 photochemically even at low concentrations. The new catalysts are faster *and also* require less overpotential to reach half of the maximum rate ($\eta_{TOF/2}$),[22] yet mechanistic studies reveal an unexpected reason for the enhancements: noncovalent self-assembly generates catalyst-rich aggregates with enhanced performance. New *monometallic* catalysts were then designed specifically to promote self-assembly in water, enabling aqueous H_2 evolution even further with enhanced activity at lower overpotential. We conclude that noncovalent catalyst self-assembly deserves consideration as a general strategy for enhancing bimetallic reactivity.

Results and Discussion

Synthesis of diiridium complexes

Diiridium complexes that covalently tether the two transition metal centers together were prepared according to Figure 2.[23] Flexible alkyl linkers were chosen to ensure that the complexes were able to reach an ideal conformation for H–H bond formation; a range of linker lengths was chosen because shorter linkers might face strain in reaching the ideal geometry, while longer linkers would likely face entropic penalties in organizing the transition state. The three new diiridium complexes **Ir_2-C12**, **Ir_2-C8**, and **Ir_2-C5** feature asymmetrically substituted bipyridine ligands that results in a statistical mixture of stereoisomers (Figure S2). The complexes were

soluble in aqueous solutions, and retain the bound chloride ligand in solution according to MS and NMR analysis.

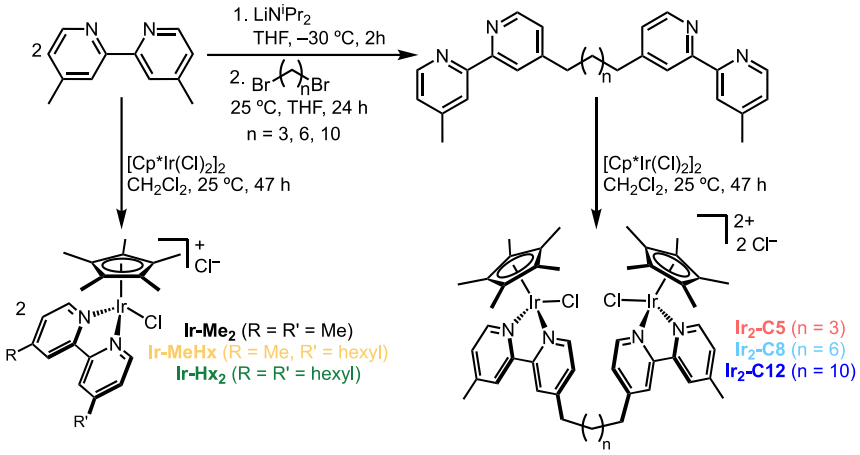

Figure 2. Synthesis of diiridium complexes.

Photoelectrocatalysis of diiridium complexes: aggregation-induced rate enhancements

The catalytic activity of the new bimetallic diiridium complexes was compared to a monometallic model complex, $[Cp^*Ir(dmbpy)Cl]^+$ (**Ir-Me$_2$**).[24] Prior studies established conditions for photoelectrocatalytic H_2 evolution from water.[16] Catalyst performance can be assessed using cyclic voltammetry (CV) and chronoamperometery (CA) to establish the activity (turnover frequency, TOF, or k_{obs} for limiting chemical step) and overpotential (the potential in excess of the thermodynamic requirement needed to reach a specific activity, η).[22] The observed rate constants vary with light intensity, cell geometry, etc., so the apparatus was kept constant across experiments to enable accurate comparisons (see methods section).

CV studies in pH 7 water (0.1 M phosphate buffer) provide initial evidence of photoelectrocatalysis mediated by the diiridium complexes. A single irreversible reduction feature is observed in the dark, exemplified by **Ir$_2$-C12** in Figure 3A, assigned as the two-electron reduction and protonation to form an iridium hydride complex (also evident by an irreversible oxidation at ca. 0.9 V vs RHE, the reversible hydrogen electrode).[16,21,24] Under 460 nm illumination, the current increased as expected for photoelectrocatalysis (Figure 3A).

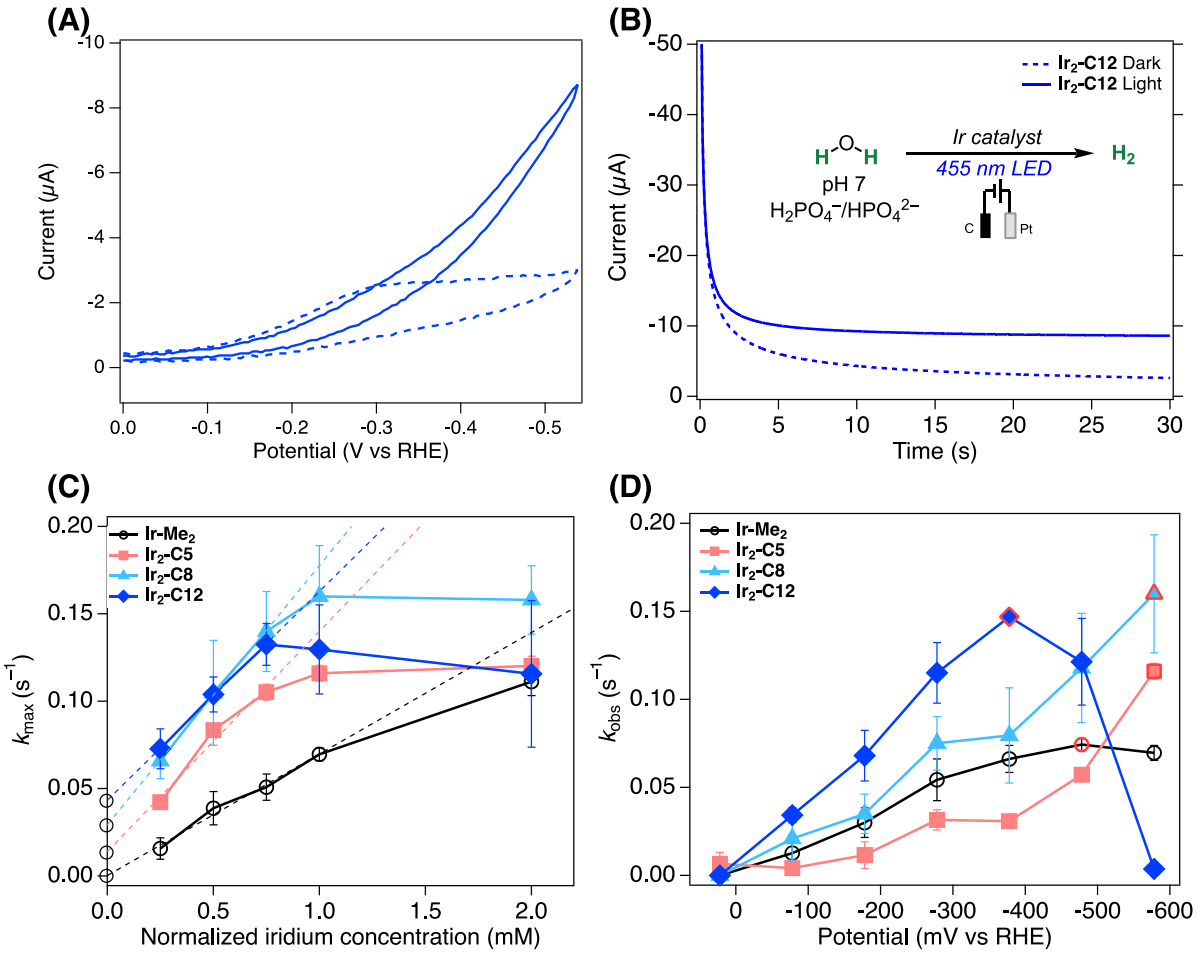

Figure 3. Electrochemical studies and photoelectrocatalytic analysis of diiridium complexes. **(A)** Cyclic voltammograms of 1 mM normalized iridium concentration **Ir$_2$-C12** in 0.1 M pH 7.0 sodium phosphate buffer protected from light (blue dashed) and under 460 nm illumination (blue solid) at 5 mV/s. **(B)** Chronoamperogram of **Ir$_2$-C12** in the dark (dotted line) and under 460 nm illumination (solid line) in 0.1 M pH 7.0 sodium phosphate buffer. **(C)** Chronoamperometry-derived maximum k_{obs} (k_{max}) vs concentration of iridium in 0.1 M pH 7.0 sodium phosphate buffer. Error bars represent standard deviation of four trials. Dashed lines are the linear fit to first 3 or 4 data points, highlighting distinct y-intercept values for each catalyst. **(D)** Observed catalytic rate constant from chronoamperometry of 1.0 mM Ir (k_{obs}) vs applied potential (vs RHE). For details of electrodes and cell configuration see the SI. Data points representing k_{max} are outlined in red.

Controlled potential electrolysis (CPE) of **Ir$_2$-C12** (at –0.28 V vs RHE) under 460 nm illumination resulted in sustained photocurrent and formation of H_2 with ca. 100% Faradaic efficiency (FE), Table S1. CPE under the same conditions but in the dark results in lower current and efficiency (FE = 21±4%). This is consistent with prior work where the charge in the dark goes

primarily towards formation of iridium hydride species that do not produce H_2 in the absence of light.[16]

With Equation S1, CA can quantify rate constants in the range relevant for photoelectrocatalysis, where rate constants below 1 s^{-1} are typical because of inherent limitations of photon flux.[8,9,25,26] Figure 3C shows the maximum catalytic rate constant (k_{max}, i.e. TOF value) as a function of normalized iridium concentration (concentration of Ir atoms, which is twice the molar concentration of diiridum complexes). The monometallic complex **Ir-Me$_2$** exhibits an increase in k_{max} with increasing concentration, before leveling off above 1 mM, just as seen in prior studies of monometallic complexes that react in a bimetallic mechanism.[16,17]

The diiridium complexes are significantly faster catalysts than monometallic **Ir-Me$_2$**, with the rate enhancement most striking at low concentrations. Extrapolation to infinite dilution via a linear fit of the first three data points reveals a non-zero y-intercept for the bimetallic catalysts (circled points in Figure 3C), which we attribute to catalysis featuring intramolecular H–H bond formation that does not require bimolecular reactions of the catalyst. The complex with the shortest linker, **Ir$_2$-C5**, has the smallest y-intercept value, suggesting that the relatively short chain in **Ir$_2$-C5** is not sufficiently flexible for facile access to the preferred H–H bond-forming geometry. The observed concentration-dependent k_{max} for diiridium complexes was surprising, and is inconsistent with our original hypothesis of rapid unimolecular H_2 release from bimetallic catalysts.

Another surprise, revealed in Figure 3D, is that the new bimetallic catalysts are both faster *and also operate at lower overpotential* than monometallic **Ir-Me$_2$**. At a representative normalized Ir concentration of 1 mM, rate–potential relationships reveal the expected increase in rate with increasingly negative applied potentials. The onset of catalysis for the bimetallic complexes occurs at lower overpotential. The bimetallic **Ir$_2$-C12** matches the maximum rate of **Ir-Me$_2$** at a 300 mV milder overpotential.

We turned next to understanding the origin of the improved performance using electrochemical and spectroscopic analysis. Voltammetric comparisons of bimetallic and monometallic complexes in pH 7 phosphate buffered water revealed two important features relevant to the reaction mechanism. First, because the wave shape is almost the same for each complex, we can conclude that there is negligible electronic communication between the metal centers (SI Section II). Second, a 170 mV anodic shift of the cathodic peak potential ($E_{p,c}$) in **Ir$_2$-C12** relative to **Ir-Me$_2$** (Figure 3A), indicated an unexpected difference in electronic structure of

local environment between the complexes. A second reduction is also apparent in **Ir$_2$-C12**, which is attributed to reduction of the electrogenerated Ir–H at unusually mild potentials; the photoelectrocatalysis shuts down once this reduction is reached, explaining the reduced activity around –0.50 V vs. RHE for this catalyst (Figure 3D). These differences are only observed in water (in acetonitrile, all complexes have almost identical reduction potentials, Figure S39), so the change in reduction potential must be related to the aqueous medium.

In fact, the new iridium complexes form catalytically active aggregates in water. Marked changes in the ^{1}H NMR spectra of **Ir$_2$-C8** and **Ir$_2$-C12** indicated a dramatic change in chemical environment with increasing concentration. NOE studies revealed extensive intermolecular through-space coupling between almost all protons, as expected for a "catalyst-only" aggregate that brings the metal complexes into close proximity (Figures S83-S85). Only modest changes in chemical shift were observed for **Ir-Me$_2$** and **Ir$_2$-C5**, and minimal NOE interactions consistent with intramolecular through-space coupling. Absorption spectra of the complexes were almost identical at low concentration, providing further support for negligible electronic communication in the bimetallic complexes. At increasing concentration, evidence of light scattering gave further evidence for bimetallic catalyst self-assembly, induced by the ambiphilic combination of a hydrophobic linker and two hydrophilic iridium cations.

Dynamic Light Scattering (DLS) can provide quantitative insight into the nature of molecular aggregates, which are modeled here as spherical micelles that place the hydrophilic positively charged iridium centers on the outside and the hydrophobic linkers on the inside (Figure 4A). The increase in scattering counts with concentration is fully consistent with aggregation of the **Ir$_2$-C8** and **Ir$_2$-C12** bimetallic complexes (Figure 4; **Ir$_2$-C5** precipitates above 2.5 mM Ir, but there is little evidence for soluble aggregates with this complex). As shown in Figure 4C, a rapid increase in particle size (assuming a spherical micelle) is observed for **Ir$_2$-C8** and **Ir$_2$-C12** as the concentration increases to about 4 mM, followed by additional increases after that as particles reach 3-5 nm diameter, with diffusion coefficients on the order of 1 x 10^{-6} $cm^2 \cdot s^{-1}$. The particle size for **Ir$_2$-C5** and **Ir-Me$_2$** remains < 1 nm throughout and the diffusion coefficient is much larger (ca. 6 x 10^{-6} $cm^2 \cdot s^{-1}$) than for **Ir$_2$-C8** and **Ir$_2$-C12**. These differences can be attributed to the catalysts with longer linkers being more hydrophobic and presenting more hydrocarbon units capable of noncovalent interactions leading to aggregation into molecularly defined nanoscale particles.

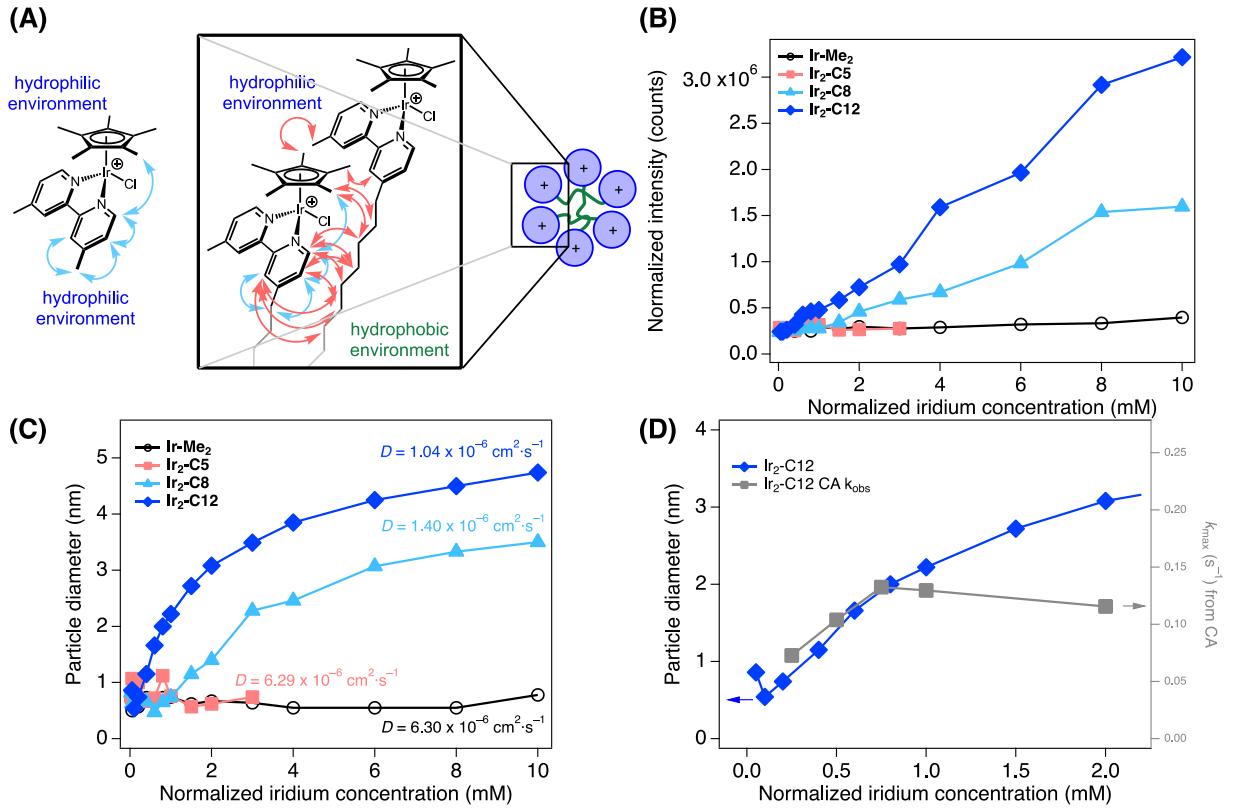

Figure 4. Self-assembly into catalytic aggregates. (A) Structure drawings highlighting how NOE interactions (blue and red double-headed arrows) can differentiate non-aggregating complexes (e.g. **Ir-Me$_2$**) and aggregating complexes (e.g. **Ir$_2$-C12**), modeled as spherical micelles. **(B)** DLS-derived plot of normalized intensity vs normalized iridium concentration. **(C)** DLS-derived plot of particle diameter vs normalized iridium concentration. **(D)** Overlay of particle diameter (blue diamonds) and k_{obs} at –0.589 V vs RHE (k_{max}, gray squares) as a function of normalized iridium concentration. **Ir-Me$_2$** (black circles), **Ir$_2$-C5** (pink squares), **Ir$_2$-C8** (teal triangles), and **Ir$_2$-C12** (blue diamonds). Conditions: 0.1 M pH 7 sodium phosphate.

The formation of nanoscale aggregates can explain all of the spectroscopic and catalytic data outlined above. The self-assembly would bring many positively charged Ir centers into close proximity, which could lead to an anodic shift in reduction potentials due to local electric field effects. The microenvironment around each Ir complex is thus dramatically different in dilute solution and in the aggregates, which affects the redox behavior. Similar shifts have been observed by covalently attaching charged groups to transition metal complexes.[27] This spatial proximity could also manifest as changes in local environment for different stereoisomers of the complexes, leading to changes in the number of observed signals, and the more hydrophobic environment can

explain the marked upfield shift in the resonances of the protons on the aliphatic linkers. The self-aggregation of hydrophobic small molecules in water has been studied extensively, usually in different context.[28] One example of a cationic organic molecule with long aliphatic substituents that shows similar NMR spectroscopic behavior are imidazolium derivatives.[29] It is rare for a catalyst to self-assemble into well-defined "catalyst only" aggregates; a more common approach has been to micelles of self-assembled catalytically inactive organic groups to provide a platform upon which to bind catalysts through non-covalent interactions.[30,31] In this case, the "catalyst only" aggregates have a unique advantage of *intrinsically requiring close proximity between catalytic sites*, leading to accelerated catalysis via a bimetallic mechanism.

The formation of micelles also helps explain the enhanced catalytic activity. The trends in extent of aggregation indicated by DLS correspond strikingly well with the trends in catalytic activity. An overlay is shown in Figure 4D. The complex **Ir$_2$-C12** forms the largest aggregates at the lowest concentration and has the fastest catalysis at lower potentials, followed by **Ir$_2$-C8**. The less active catalysts **Ir$_2$-C5** and **Ir-Me$_2$** both have limited aggregation. We hypothesize that micelles support faster catalysis by dramatically increasing the local Ir concentration. The numerous proximal metal centers could enable rapid sampling of a large number of geometric orientations, facilitating H–H coupling. The data suggests that bimetallic H–H coupling to release H_2 is more facile at the Ir-rich surface of the micelle than in dilute solution via intramolecular reactivity of a single diiridium complex. This in turn implies that the long alkyl linkers are too flexible for efficient intramolecular reactivity, perhaps due to a high entropic penalty to bringing the two Ir–H units close together and reach the proper orientation for H–H coupling.

Self-assembly of catalytic micelles from monometallic complexes with hydrophobic groups

If noncovalent interactions can drive self-assembly into highly active micelles composed of well-defined molecular catalysts, monometallic catalysts with hydrophobic functional groups should generate similar self-assembled aggregates capable of efficient light-driven H_2 evolution. Following Figure 2 above, [Cp*Ir(mhbpy)Cl][Cl] (**Ir-MeHx)**, with a methyl group on one pyridine and a hexyl tail on the other, and [Cp*Ir(dhbpy)Cl][Cl] (**Ir-Hx$_2$**), with hexyl tails on both pyridines, were prepared for study.

Comparative electrochemical and spectroscopic studies were undertaken to assess the aggregation propensities of the two new monometallic complexes. As shown in Figure 5A, the $E_{p,c}$

of **Ir-Hx2** is anodically shifted by 180 mV compared to **Ir-Me2** in buffer solution. The shift, coupled with the almost exact match in $E_{p,c}$ for these two complexes in MeCN, provides strong initial evidence for micelle formation. A much smaller anodic shift is apparent for **Ir-MeHx**, suggesting less aggregation in the complex with only one hydrophobic tail. DLS are consistent with substantial aggregation with the **Ir2-C8**, **Ir2-C12**, and **Ir-Hx2** complexes. The two-tailed complex forms micelles of similar diameter at similar concentrations as the bimetallic complex with the longest tether, **Ir2-C12** (Figure 5C/D). The one-tailed complex **Ir-MeHx** showed evidence of aggregation by DLS, but the data had higher scatter than for other samples. Therefore, we also obtained diffusion coefficients using CA, and find good agreement between methods and more reliable data for **Ir-MeHx** (Table S2). The electrochemically determined diffusion coefficients also indicate that the whole micelle is diffusing as a unit up to the electrode surface, rather than dynamically breaking up into unimolecular units that mediate electrochemistry.

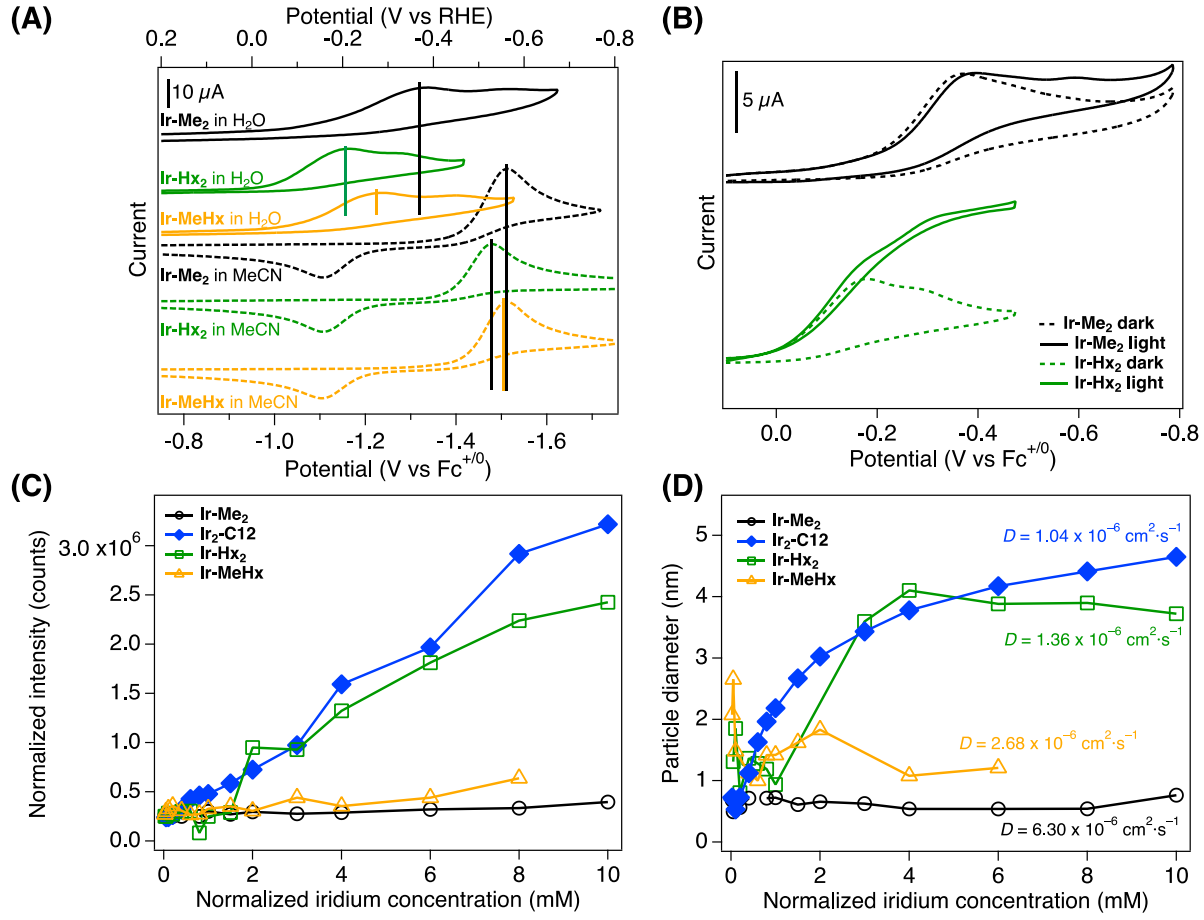

Figure 5. Electrochemistry, photoelectrocatalysis, and aggregation characterization of monometallic self-aggregating catalysts as compared to other catalysts in this study. **(A)** Cyclic voltammograms of **Ir-Me2** (black solid line), **Ir-Hx2** (green solid line) and **Ir-MeHx** (yellow solid

line) in 0.1 M pH 7.0 sodium phosphate buffer and **Ir-Me$_2$** (black dotted line), **Ir-Hx$_2$** (green dotted line), and **Ir-MeHx** (orange dotted line) in MeCN. The vertical black lines represent $E_{p,c}$ of each complex in the respective solvent. **(B)** Cyclic voltammograms of **Ir-Me$_2$** (black line), **Ir-Hx$_2$** (green line), and **Ir-MeHx** (yellow line) in the dark (solid lines) and under 460 nm illumination (dotted lines) in 0.1 M pH 7.0 sodium phosphate buffer at 25 mV/s. **(C)** DLS-derived normalized intensity vs normalized iridium concentration plot. **(D)** DLS-derived particle diameter vs normalized iridium concentration plot. **Ir-Me$_2$** (black circles) **Ir$_2$-C12** (blue diamonds), **Ir-Hx$_2$** (green squares) and **Ir-MeHx** (yellow triangles). Conditions: 0.1 M pH 7 sodium phosphate buffer, for details see methods section.

Figure 6 summarizes the CA data. One-tailed **Ir-MeHx** has almost identical behavior to the original complex **Ir-Me$_2$**, as expected considering that neither complex aggregates. Two-tailed **Ir-Hx$_2$**, conversely, aggregates extensively and also exhibits dramatically improved activity. Extrapolating the k_{max} vs concentration plots to infinite dilution shows that the two monometallic "tailed" complexes have a y-intercept at zero. This is expected for a monometallic catalyst, as at the lowest concentrations the degree of aggregation will be low, and there is no intramolecular coupling mechanism available as in the bimetallic catalysts. The self-assembly of **Ir-Hx$_2$** leads to rapid rate increases that correlate with the concentration dependence of the aggregation. CPE at –0.28 V vs RHE under 460 nm illumination produced H_2 in quantitative Faradaic efficiency (Table S1). Thus, **Ir-Hx$_2$** has the highest activity of all of the complexes studied, with k_{max} up to 5 times higher than the monometallic complexes that do not form micelles. Figure 6C illustrates the highly unusual behavior of increasing activity at lower overpotential, breaking the usual scaling relationship of higher activity at higher overpotential.[22,32–34] The self-assembling catalyst **Ir-Hx$_2$** reaches the same activity as **Ir-Me$_2$** (ca. 0.05 s^{-1}) at more than 400 mV lower overpotential.

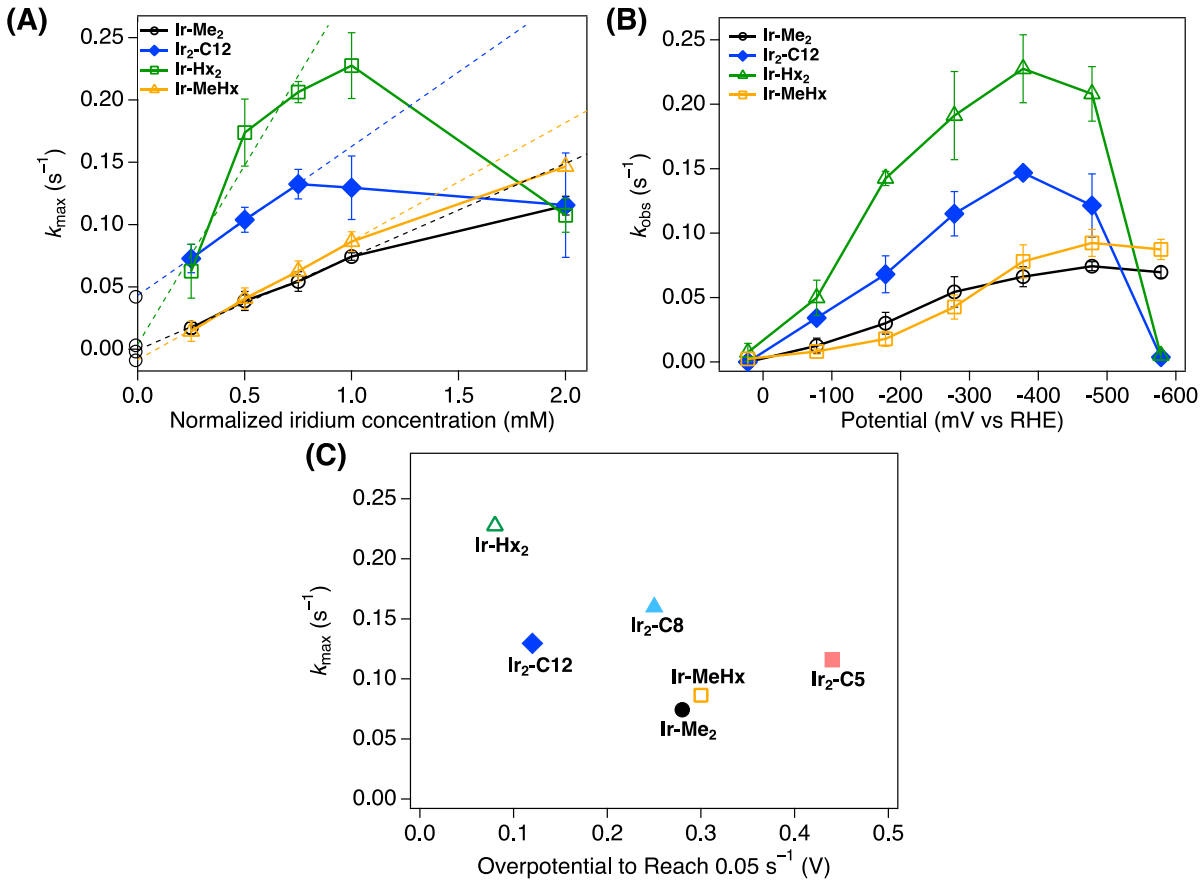

Figure 6. Activity overpotential relationships. (A) Chronoamperometry-derived observed catalytic rate at potential with maximum k_{obs} (k_{max}) vs normalize iridium concentration in 0.1 M pH 7.0 sodium phosphate buffer. Dashed lines are the linear fit to first 3 or 4 data points, highlighting distinct y-intercept values for each catalyst. **(B)** Chronoamperometry-derived observed catalytic rate of 1.0 mM Ir (k_{obs}) vs applied potential vs RHE in 0.1 M pH 7.0 sodium phosphate buffer. **(C)** Activity vs overpotential plot showing no linear relationship. **Ir-Me2** (open black circles), **Ir2-C12** (filled blue diamonds), **Ir-Hx2** (open green triangles) and **Ir-MeHx** (open yellow squares). Error bars represent standard deviation of four trials.

Conclusion

Bimetallic iridium catalysts that act as both the light absorber and the fuel-forming catalyst produce H_2 approximately five times faster than monometallic analogues while also operating at lower overpotentials. The origin of the improvement *is not rapid intramolecular H–H coupling as originally predicted*, but rather self-assembly into micelles comprised entirely of the catalyst. The aggregates place many cationic iridium centers in close proximity at the periphery, leading to

milder reduction potentials due to nearby positive charges (lowering overpotential) and facilitating neighboring Ir–H species to reach the appropriate geometry for H–H coupling and H_2 release (accelerating rate). The same design principles are equally applicable to monometallic iridium complexes with hydrophobic groups. The monometallic catalyst with two hydrophobic substituents was the top performer of all the catalysts, reaching ca. 10-fold higher rates of H_2 evolution while operating at as much as ca. 400 mV lower overpotential than the control catalyst. This catalyst system operates in neutral water at overpotentials approaching the thermodynamic potential for H_2 evolution and with rates approaching the limiting values expected for typical solar photon flux conditions.

There is a rich history of utilizing noncovalent interactions in catalysis.[30,35–38] One approach has utilized organic micelles or lipid bilayers as scaffolds to compartmentalize or immobilize catalytic species.[30,31,39] The aggregation described here is distinct, instead relying on self-assembly of the catalyst itself. This leads to aggregates with maximal local concentrations of catalyst, ideal for bimetallic reactions. The high local concentration also leads to microenvironment effects, reflected in the modulated reduction potentials. The self-assembly of catalysts themselves into larger aggregates is less explored than the using inert assemblies as supporting scaffolds for catalysts. One recent example of catalyst self-assembly of water oxidation via bimetallic O–O coupling explored similar strategies,[40] although in that case the activity was actually lower in the aggregates than in the original monometallic catalyst. We hypothesize that similar noncovalent catalyst self-assembly tactics could be utilized for other catalysts that feature a bimetallic mechanism, which is commonly encountered in various fields of catalysis.

Acknowledgements

This work was supported by the U.S. Department of Energy, Office of Science, Office of Basic Energy Sciences, under Award DE-SC0014255. The NMR spectroscopy was supported by the National Science Foundation under Grant CHE-1828183. The mass spectrometry was supported by the National Science Foundation under Grant CHE-1726291. The authors acknowledge Nuwanthika Kumarage for assistance with NMR spectral acquisition. Dr. Ashutosh Tripathy, Director of the Macromolecular Interactions Facility where the DLS experiments were performed, is also acknowledge for experimental assistance. The DLS experimental work was supported by the National Cancer Institute of the National Institutes of Health under award number

P30CA016086. The content is solely the responsibility of the authors and does not necessarily represent the official views of the National Institutes of Health.

References

1. Lewis, N. S. & Nocera, D. G. Powering the planet: Chemical challenges in solar energy utilization. *Proc. Natl. Acad. Sci.* **103**, 15729–15735 (2006).
2. Walter, M. G. *et al.* Solar Water Splitting Cells. *Chem. Rev.* **110**, 6446–6473 (2010).
3. Cook, T. R. *et al.* Solar Energy Supply and Storage for the Legacy and Nonlegacy Worlds. *Chem. Rev.* **110**, 6474–6502 (2010).
4. Tachibana, Y., Vayssieres, L. & Durrant, J. R. Artificial photosynthesis for solar water-splitting. *Nat. Photonics* **6**, 511–518 (2012).
5. Esswein, A. J. & Nocera, D. G. Hydrogen Production by Molecular Photocatalysis. *Chem. Rev.* **107**, 4022–4047 (2007).
6. Berardi, S. *et al.* Molecular artificial photosynthesis. *Chem Soc Rev* **43**, 7501–7519 (2014).
7. Kärkäs, M. D., Verho, O., Johnston, E. V. & Åkermark, B. Artificial Photosynthesis: Molecular Systems for Catalytic Water Oxidation. *Chem. Rev.* **114**, 11863–12001 (2014).
8. Ashford, D. L. *et al.* Molecular Chromophore–Catalyst Assemblies for Solar Fuel Applications. *Chem. Rev.* **115**, 13006–13049 (2015).
9. Brereton, K. R., Bonn, A. G. & Miller, A. J. M. Molecular Photoelectrocatalysts for Light-Driven Hydrogen Production. *ACS Energy Lett.* **3**, 1128–1136 (2018).
10. Reyes Cruz, E. A. *et al.* Molecular-Modified Photocathodes for Applications in Artificial Photosynthesis and Solar-to-Fuel Technologies. *Chem. Rev.* **122**, 16051–16109 (2022).
11. Costentin, C., Dridi, H. & Savéant, J.-M. Molecular Catalysis of H 2 Evolution: Diagnosing Heterolytic versus Homolytic Pathways. *J. Am. Chem. Soc.* **136**, 13727–13734 (2014).

12. Dempsey, J. L., Brunschwig, B. S., Winkler, J. R. & Gray, H. B. Hydrogen Evolution Catalyzed by Cobaloximes. *Acc. Chem. Res.* **42**, 1995–2004 (2009).
13. Valdez, C. N., Dempsey, J. L., Brunschwig, B. S., Winkler, J. R. & Gray, H. B. Catalytic hydrogen evolution from a covalently linked dicobaloxime. *Proc. Natl. Acad. Sci.* **109**, 15589–15593 (2012).
14. Han, Y. *et al.* Singly versus Doubly Reduced Nickel Porphyrins for Proton Reduction: Experimental and Theoretical Evidence for a Homolytic Hydrogen-Evolution Reaction. *Angew. Chem. Int. Ed.* **55**, 5457–5462 (2016).
15. Guo, X. *et al.* Homolytic versus Heterolytic Hydrogen Evolution Reaction Steered by a Steric Effect. *Angew. Chem. - Int. Ed.* **59**, 8941–8946 (2020).
16. Pitman, C. L. & Miller, A. J. M. Molecular photoelectrocatalysts for visible light-driven hydrogen evolution from neutral water. *ACS Catal.* **4**, 2727–2733 (2014).
17. Stratakes, B. M. & Miller, A. J. M. H2Evolution at an Electrochemical 'underpotential' with an Iridium-Based Molecular Photoelectrocatalyst. *ACS Catal.* **10**, 9006–9018 (2020).
18. Rivier, L. *et al.* Photoproduction of Hydrogen by Decamethylruthenocene Combined with Electrochemical Recycling. *Angew. Chem. Int. Ed.* **56**, 2324–2327 (2017).
19. Rivier, L. *et al.* Mechanistic Study on the Photogeneration of Hydrogen by Decamethylruthenocene. *Chem. – Eur. J.* **25**, 12769–12779 (2019).
20. Huang, J., Sun, J., Wu, Y. & Turro, C. Dirhodium(II,II)/NiO Photocathode for Photoelectrocatalytic Hydrogen Evolution with Red Light. *J. Am. Chem. Soc.* (2021) doi:10.1021/jacs.0c12171.

21. Chambers, M. B., Kurtz, D. A., Pitman, C. L., Brennaman, M. K. & Miller, A. J. M. Efficient Photochemical Dihydrogen Generation Initiated by a Bimetallic Self-Quenching Mechanism. *J. Am. Chem. Soc.* **138**, 13509–13512 (2016).
22. Stratakes, B. M., Dempsey, J. L. & Miller, A. J. M. Determining the Overpotential of Electrochemical Fuel Synthesis Mediated by Molecular Catalysts: Recommended Practices, Standard Reduction Potentials, and Challenges. *ChemElectroChem* **8**, 4161–4180 (2021).
23. Dadci, L. *et al.* π-Arene Aqua Complexes of Cobalt, Rhodium, Iridium, and Ruthenium: Preparation, Structure, and Kinetics of Water Exchange and Water Substitution. *Inorg. Chem.* **34**, 306–315 (1995).
24. Pitman, C. L., Brereton, K. R. & Miller, A. J. M. Aqueous Hydricity of Late Metal Catalysts as a Continuum Tuned by Ligands and the Medium. *J. Am. Chem. Soc.* **138**, 2252–2260 (2016).
25. Wadsworth, B. L., Beiler, A. M., Khusnutdinova, D., Reyes Cruz, E. A. & Moore, G. F. Interplay between Light Flux, Quantum Efficiency, and Turnover Frequency in Molecular-Modified Photoelectrosynthetic Assemblies. *J. Am. Chem. Soc.* **141**, 15932–15941 (2019).
26. Nguyen, N. P., Wadsworth, B. L., Nishiori, D., Reyes Cruz, E. A. & Moore, G. F. Understanding and Controlling the Performance-Limiting Steps of Catalyst-Modified Semiconductors. *J. Phys. Chem. Lett.* **12**, 199–203 (2021).
27. Weberg, A. B., Murphy, R. P. & Tomson, N. C. Oriented internal electrostatic fields: an emerging design element in coordination chemistry and catalysis. *Chem. Sci.* **13**, 5432–5446 (2022).
28. Jiang, X. Hydrophobic-lipophilic interactions. Aggregation and self-coiling of organic molecules. *Acc. Chem. Res.* **21**, 362–367 (1988).

29. Blesic, M. *et al.* Self-aggregation of ionic liquids: micelle formation in aqueous solution. *Green Chem.* **9**, 481 (2007).
30. Keijer, T., Bouwens, T., Hessels, J. & Reek, J. N. H. Supramolecular strategies in artificial photosynthesis. *Chem. Sci.* **12**, 50–70 (2021).
31. Pannwitz, A. *et al.* Roadmap towards solar fuel synthesis at the water interface of liposome membranes. *Chem. Soc. Rev.* **50**, 4833–4855 (2021).
32. Wang, Y.-H. *et al.* Brønsted Acid Scaling Relationships Enable Control Over Product Selectivity from O 2 Reduction with a Mononuclear Cobalt Porphyrin Catalyst. *ACS Cent. Sci.* **5**, 1024–1034 (2019).
33. Martin, D. J., Wise, C. F., Pegis, M. L. & Mayer, J. M. Developing Scaling Relationships for Molecular Electrocatalysis through Studies of Fe-Porphyrin-Catalyzed O $_2$ Reduction. *Acc. Chem. Res.* **53**, 1056–1065 (2020).
34. Nie, W. & McCrory, C. C. L. Strategies for breaking molecular scaling relationships for the electrochemical CO $_2$ reduction reaction. *Dalton Trans.* **51**, 6993–7010 (2022).
35. Boulas, P. L., Go, M. & Echegoyen, L. Electrochemistry of supramolecular systems. *Angew. Chem. Int. Ed.* **37**, 216–247 (1998).
36. Wiester, M. J., Ulmann, P. A. & Mirkin, C. A. Enzyme mimics based upon supramolecular coordination chemistry. *Angew. Chem. - Int. Ed.* **50**, 114–137 (2011).
37. Raynal, M., Ballester, P., Vidal-Ferran, A. & van Leeuwen, P. W. N. M. Supramolecular catalysis. Part 1: non-covalent interactions as a tool for building and modifying homogeneous catalysts. *Chem. Soc. Rev.* **43**, 1660 (2014).
38. Raynal, M., Ballester, P., Vidal-Ferran, A. & van Leeuwen, P. W. N. M. Supramolecular catalysis. Part 2: artificial enzyme mimics. *Chem Soc Rev* **43**, 1734–1787 (2014).

39. Zeng, T. *et al.* Hybrid bilayer membranes as platforms for biomimicry and catalysis. *Nat. Rev. Chem.* **6**, 862–880 (2022).

40. Yang, B. *et al.* Self-Assembled Amphiphilic Water Oxidation Catalysts: Control of O−O Bond Formation Pathways by Different Aggregation Patterns. *Angew. Chem. Int. Ed.* **55**, 6229–6234 (2016).